

## **Chapter 2**

### **Review of Diffuse Optical Tomography:**

#### **Theory and Tissue Optics**

The propagation of photons through turbid media such as biological tissue can be modeled as a diffusion process [1-20]. The direction and polarization state of photons entering the tissue quickly becomes randomized by multiple scattering events. A pulse of photons on the order of a picosecond incident on a slab, will be spread out in time due to the diffusion of photons as it propagates through and exits the slab. The resulting temporal point spread function (TPSF) can be modeled by the diffusion approximation to the radiative transport equation. Analytical models have been developed for simple geometries such as the infinite homogeneous slab with boundary conditions applicable to breast imaging in transmission [1-3,6]. This chapter begins with a review of the theory of diffuse optical tomography as it applies to optical breast imaging in the time-domain in the transmission geometry.

An understanding of the anatomy specific to normal breast tissue and of benign and cancerous lesions of the breast is important for accurate modeling and assessment of optical breast imaging. Section 2.2 reviews the important distinctions between different types of tissue that comprise the human female breast. The features of benign and cancerous tumors of the breast are discussed along with anticipated optical contrast associated with the tumors and neighboring tissues. The primary chromophores relevant to optical imaging of the breast in the near infrared are discussed. It has been shown that

the effects of lipids and water on the absorption coefficient should not be neglected due to their relative abundance in the breast along with the generally lower concentrations of hemoglobin relative to other tissue types [23,24].

## **2.1 Theory of Diffuse Optical Tomography**

The diffusion approximation to the radiative transport equation is the most widely used model to describe the migration of light through biological tissues. The Time-Domain Optical Breast Imaging System described in this dissertation is based on a slab geometry. Thus, time-dependant solutions to the diffusion approximation are discussed for the homogeneous infinite slab along with the relative merits of various boundary conditions. The challenge of DOT is that of imaging heterogeneities in the tissue that may be due to functional changes in the tissue indicative of cancer or benign lesions. The homogenous solutions of the diffusion approximation can be used in a perturbation approach to derive approximate analytical solutions to the heterogeneous problem. The linear first Born approximation that has been widely used in optical tomography is reviewed. This section closes with a discussion of the inverse problem and image reconstruction techniques.

### **2.1.1 The Radiative Transfer Equation**

The most general model for light transport that may be given is the theory of radiative transfer, or photon transport theory, which has been extensively studied in atmospheric physics, and in neutron transport [1,2].

The radiative transfer equation, also referred to as the Boltzmann transport equation, is the expression of the balance of energy inside a volume element of the scattering medium. Generally, only elastic scattering is considered, that is a scattering event

changes the direction of the photon, not the frequency [3]. This also implies that the absorbed energy is completely lost in the sense that it is converted to kinetic energy manifest as heat. The equation describes the behavior of the specific intensity  $I(\mathbf{r}, t, \hat{s})$  with units of  $\text{Wm}^{-2}\text{sr}^{-1}$ , i.e., the energy moving in the direction  $\hat{s}$ , per unit solid angle, per unit time, and per unit area normal to the  $\hat{s}$  direction. The radiative transfer equation can be obtained by considering the total space and time variation of the radiance along a direction  $\hat{s}$  in an elementary volume and making this equal to the variation of specific intensity due to scattering and absorption inside the medium. The final equation for the time-dependent case [1-4] is

$$\frac{1}{v} \frac{\partial}{\partial t} I(\mathbf{r}, t, \hat{s}) + \hat{s} \cdot \nabla I(\mathbf{r}, t, \hat{s}) = -\mu_t I(\mathbf{r}, t, \hat{s}) + \frac{\mu_s}{4\pi} \int_{4\pi} p(\hat{s}, \hat{s}') I(\mathbf{r}, t, \hat{s}') d\hat{s}' + S(\mathbf{r}, t, \hat{s}) \quad (2.1)$$

where  $v$  is the speed of light inside the diffusing medium defined by  $v = c/n$ , where  $c$  is the speed of light in vacuum and  $n$  is the effective index of the medium,  $\mu_t = \mu_s + \mu_a$  is the extinction coefficient where  $\mu_s$  and  $\mu_a$  are the scattering and absorption coefficients respectively (the inverse of  $\mu_s$  and  $\mu_a$  represent the mean path between two consecutive scattering events and the mean path between two absorption events, respectively),  $S(\mathbf{r}, t, \hat{s})$  is the source term representing the spatial and angular distribution of the source in units of  $\text{Wm}^{-3}\text{sr}^{-1}$ , and  $p(\hat{s}, \hat{s}')$  is the scattering function that defines the probability of a photon moving in the direction  $\hat{s}$  to be scattered into direction  $\hat{s}'$ . The scattering function was normalized according to [3]

$$\int_{4\pi} p(\hat{s}, \hat{s}') d\hat{s}' = \frac{4\pi\mu_s}{\mu_t} \quad (2.2)$$

If the source term is assumed to be a Dirac delta function, the solution represents the Green's function of the problem from which the solution for a generic source can be

obtained with convolution integrals. In the time-domain, the Green's function is referred to as the Temporal Point Spread Function (TPSF) having a damped exponential form that is limited by the absorption coefficient. The source term of unit strength is thus represented by

$$S(\mathbf{r}, t, \hat{s}) = \delta(\mathbf{r}) \delta(\hat{s}) \delta(t) \quad (2.3).$$

If  $I(\mathbf{r}, t, \hat{s})|_{\mu_a=0}$  is a solution of Equation (2.1) for a nonabsorbing medium with the source term described by a Dirac delta function, then

$$I(\mathbf{r}, t, \hat{s}) = \exp(-\mu_a \nu t) I(\mathbf{r}, t, \hat{s})|_{\mu_a=0} \quad (2.4)$$

is the solution to the same equation when the absorption coefficient (independent of  $\mathbf{r}$ ) is  $\mu_a$ . The validity can be checked [4] by substitution of Equation (2.4) into Equation (2.1) with the assumption that the source term is zero except at  $\mathbf{r} = 0$ , giving

$$\frac{1}{\nu} \frac{\partial}{\partial t} I_0(\mathbf{r}, t, \hat{s}) + \hat{s} \cdot \nabla I_0(\mathbf{r}, t, \hat{s}) = -\mu_t I_0(\mathbf{r}, t, \hat{s}) + \frac{\mu_t}{4\pi} \int_{4\pi} p(\hat{s}, \hat{s}') I_0(\mathbf{r}, t, \hat{s}) d\hat{s}' \quad (2.5)$$

where the zero subscript has been used to denote the solution for  $\mu_a = 0$ . Thus, the time-dependent impulse response of a homogeneous medium has two separable parts [4]: one that is determined by the scattering coefficient [ $I_0(\mathbf{r}, t, \hat{s})$ ] and one that is determined by the medium absorption [ $\exp(-\mu_a \nu t)$ ]. Diffusion theory is derived from transport theory and would therefore be expected to have the same transformation property [4]. This property is made use of in the next section for which the diffusion approximation to the radiative transport equation is introduced.

### 2.1.2 Diffusion Approximation to the Radiative Transport Equation

The radiative transport equation is complicated and it is almost impossible to obtain analytical solutions with a degree of generality that can be applied to solving real problems. Numerical methods or analytical approximations are generally used. The analytical model most widely used is the diffusion approximation. The radiative transport equation can be simplified by an expansion in spherical harmonics [1,4]. The result is a set of  $(N+1)^2$  coupled partial differential equations known as the  $P_N$  approximation. For odd  $N$ , such equations may be reduced to a single  $(N+1)$ th-order differential equation. The  $P_1$  approximation to the radiative transport equation is generally referred to as the diffusion approximation given by

$$\left( -D\nabla^2 + \nu\mu_a + \frac{\partial}{\partial t} \right) \Phi(\mathbf{r}, t) = \nu S(\mathbf{r}, t) \quad (2.6)$$

where  $D = \nu / (3\mu_s')$  is the photon diffusion coefficient [ $\text{cm}^2/\text{s}$ ],  $\mu_s'$  is the reduced scattering coefficient [ $\text{cm}^{-1}$ ], which is the reciprocal of the random walk length, that is the average length for a photon's direction to become random,  $\Phi(\mathbf{r}, t)$  is the photon fluence rate [ $\text{Wcm}^{-2}$ ], and  $S(\mathbf{r}, t)$  is the source term [ $\text{Wcm}^{-3}$ ]. The scattering coefficient and the reduced scattering coefficient are related by

$$\mu_s' = \mu_s (1 - g) \quad (2.7)$$

where  $g$  is the single-scattering anisotropy factor, which is a measure of the fraction of photons scattered in the forward direction [3] given by

$$g = \langle \cos(\theta) \rangle = \frac{\int (\hat{s} \cdot \hat{s}') p(\hat{s} \cdot \hat{s}') d\hat{s}'}{\int_{4\pi} p(\hat{s} \cdot \hat{s}') d\hat{s}'} \quad (2.8).$$

Typical tissues, such as breast, scatter predominately in the forward direction with a value of  $g$  on the order of 0.9 [5]. Thus for a scattering length in the breast on the order of 0.100 mm, the random walk step would be 1 mm, meaning that it takes about 10 scattering events for the photon direction to become random relative to its initial direction. The  $P_1$  approximation is valid when the albedo  $c = \mu_s / (\mu_s + \mu_a)$  is close to unity, i.e.,  $\mu_a \ll \mu_s$ , the normalized scattering function is not too anisotropic, and the source-detector separation is large compared to the random walk length [4].

Many authors show a dependency of the diffusion coefficient on the absorption coefficient as  $D = v/3(\mu_s + \mu_a)$  [2,6,8,9]. The diffusion coefficient independent of  $\mu_a$  was first considered by Furustu in 1980 and Furutsu and Yamada in 1994 [3]. More recently, Durduran in 1997 [10] and Contini in 1997 [3] compared solutions of the radiative transport equation obtained by Monte Carlo simulations, showing that for large values of  $\mu_a$ , better agreement is obtained when the diffusion coefficient independent of  $\mu_a$  is assumed. This is also consistent with the assumption of the  $P_1$  approximation that  $\mu_a \ll \mu_s$ .

In practical applications such as measurements on biological tissues, the photon fluence  $\phi(\mathbf{r}, t)$  is not measured directly. The measurable quantity is given by a directional component of the photon current density  $\mathbf{J}$  [photons/cm<sup>2</sup>/sec] as a statement of Fick's law according to [2,3]

$$\mathbf{J}(\mathbf{r}, t) = -D\nabla\phi(\mathbf{r}, t) \quad (2.9)$$

where Fick's law states that photons propagate predominately from areas of higher to lower photon density. In the case of measuring the transmitted intensity of breast tissue

compressed between plates, we are interested in the transmission, which is related to Equation (2.9) by

$$\mathbf{T}(\rho, t) = \left| -D\nabla\phi(\rho, z = d, t) \right| \quad (2.10)$$

where  $\rho$  is the distance in the plane of the slab from the source and  $d$  is the thickness of the slab.

### 2.1.3 Solutions of the Diffusion Equation for a Slab

The boundary conditions particular to slab geometry are used to find the Green's function solution to the time-dependent diffusion equation for the transmission case. The boundary conditions must take proper account of the air-tissue interface. They cannot be expressed exactly in closed analytical form, so three basic approximations have been used with varying degrees of complexity and validity [2,3,6]. The most complex boundary condition is known as the partial current boundary condition (PCB). The PCB makes the reasonable assumption that the photons leaving the scattering medium through the air-tissue interface do not return to the medium. This implies that the total diffuse flux inwardly directed should be equal to zero at the surface. The solutions are rather complex and have shown no significant advantage over the simpler, but more approximate, extrapolated boundary condition (EBC). The EBC approximates the PCB, assuming linear behavior of the average diffuse intensity around the geometrical boundaries. The EBC assumes the average diffuse intensity to be zero at an extrapolated boundary outside the turbid medium at a distance  $z_e$  given by

$$z_e = 2A \frac{D}{\nu} \quad (2.11)$$

where the coefficient  $A$  takes account of the Fresnel reflection at the air-tissue interface and is given by [3]

$$A = \frac{1 + 3 \int_0^{2\pi} R(\theta_i) \cos^2(\theta_i) \sin(\theta_i) d\theta_i}{1 - 2 \int_0^{2\pi} R(\theta_i) \cos(\theta_i) \sin(\theta_i) d\theta_i} \quad (2.12)$$

where the Fresnel reflection coefficient for unpolarized light is given by

$$R(\theta) = \frac{1}{2} \left\{ \left[ \frac{n \cos(\theta_i) - \cos(\theta_t)}{n \cos(\theta_i) + \cos(\theta_t)} \right]^2 + \left[ \frac{\cos(\theta_i) - n \cos(\theta_t)}{\cos(\theta_i) + n \cos(\theta_t)} \right]^2 \right\} \quad (2.13)$$

and where  $n = n_2/n_1$  is the relative refractive index, which is the ratio between the refractive index of the medium and that of the external medium,  $\theta_i$  is the angle of incidence of the radiation and  $\theta_t = \arcsin[n \sin(\theta_i)]$  is the refracted angle. The integrals in Equation (2.12) are complex, but have been fit by Contini *et al.* to have the form

$$A_{fit} = 504.332889 - 2641.00214n + 5923.699064n^2 - 7376.355814n^3 \quad (2.14)$$

$$5507.53041n^4 - 2463.357945n^5 + 610.956547n^6 - 64.8047n^7$$

The error between the exact calculation of  $A$  and  $A_{fit}$  has been shown to be far below 0.05% for values of  $n$  ranging between 1.0 and 1.6. The zero boundary condition (ZBC) is the most simple and approximate of the three and assumes the average diffuse intensity equal to zero at the physical boundary. With the ZBC it is not possible to take proper account of the effect of reflection at the boundary.

The geometry applicable to an infinite slab is pictured in Figure 2.1. The photons are incident on the surface of the slab at  $z = 0$ . The scattered photons are remitted from the surface of the slab of thickness  $d$ , a distance  $\rho$  from the  $z$ -axis. The index of refraction of the slab is  $n_2$  and that of the surrounding medium,  $n_1$ .



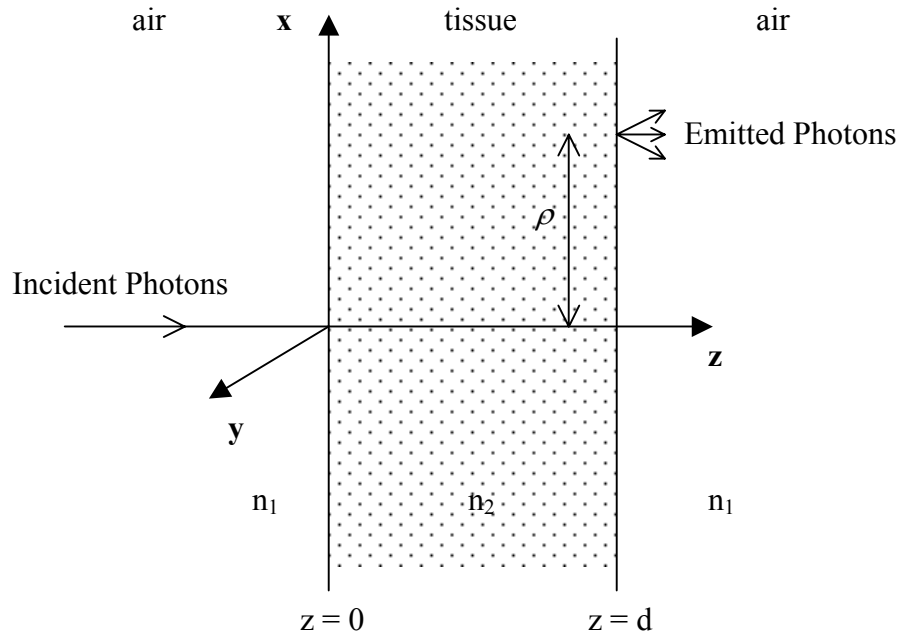
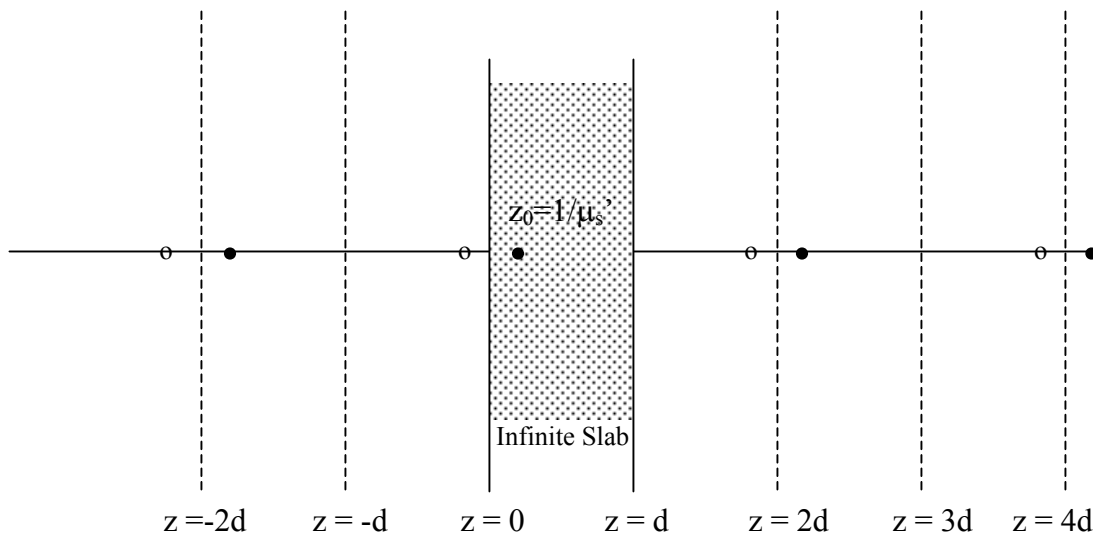


Figure 2.1 The geometry of an infinite tissue slab of thickness  $d$  is shown. The photons are incident at the origin and are emitted from the surface at a distance  $\rho$  from the source in the plane of the phantom at  $z = d$ . The tissue has an index  $n_2$  relative to the region at  $z < 0$  and  $z > d$  with index  $n_1$ .

The Green's functions for both the ZBC and the EBC will be shown. The limitations of the ZBC relative to the EBC will be discussed relative to transmission geometry. With reference to Figure 2.1, a narrow collimated pulsed laser beam is normally incident on the surface of the diffusing slab. The pulse is assumed to be mathematically described by the Dirac delta function at a time  $t = 0$ , and it is assumed to be a thin collimated (pencil) beam [3]. This is a good approximation to the real case of an ultrashort pulsed laser with dimensions that are negligible with respect to other geometrical dimensions of the problem. The diffusion equation, however, was with reference to an isotropic source. Many methods have been used to approximate the pencil beam of the diffusion equation with varying degrees of complexity. A useful simplifying assumption is that all the

incident photons are initially scattered isotropically at a depth  $z_0 = 1/\mu_s'$  below the surface.

The geometry for the calculation of the time resolved transmittance for a homogeneous slab for the ZBC is shown in Figure 2.2. The average diffuse intensity is set to zero at the surface of the slab at  $z = 0$ . As stated above, the source is assumed to be located a distance  $z_0$  into the medium. Thus a negative image source must be located at the distance  $z = -z_0$  to meet the boundary condition. The boundary condition for the



- **Positive Source**
- Negative Source

Figure 2.2 The source position is shown a distance  $z_0$  inside the tissue boundary for the zero boundary condition (ZBC). The average intensity is assumed zero at the boundary. A negative image charge is shown reflected about the  $z = 0$  boundary. The first four dipole sources are shown as part of an infinite series of dipoles.

surface located at  $z = d$  is satisfied by the dipole centered about  $z = 2d$ , but then the boundary condition at  $z = 0$  is violated for  $t > 2d/v$ . Both boundary conditions can only be met simultaneously by adding an infinite number of dipoles [1,3,6]. In practice, the number of dipoles required depends on the background optical properties of the slab and

the maximum time for which the transmittance is calculated. The Green's function for the transmittance of an infinite slab with the ZBC is given by Patterson *et al.* [6] as

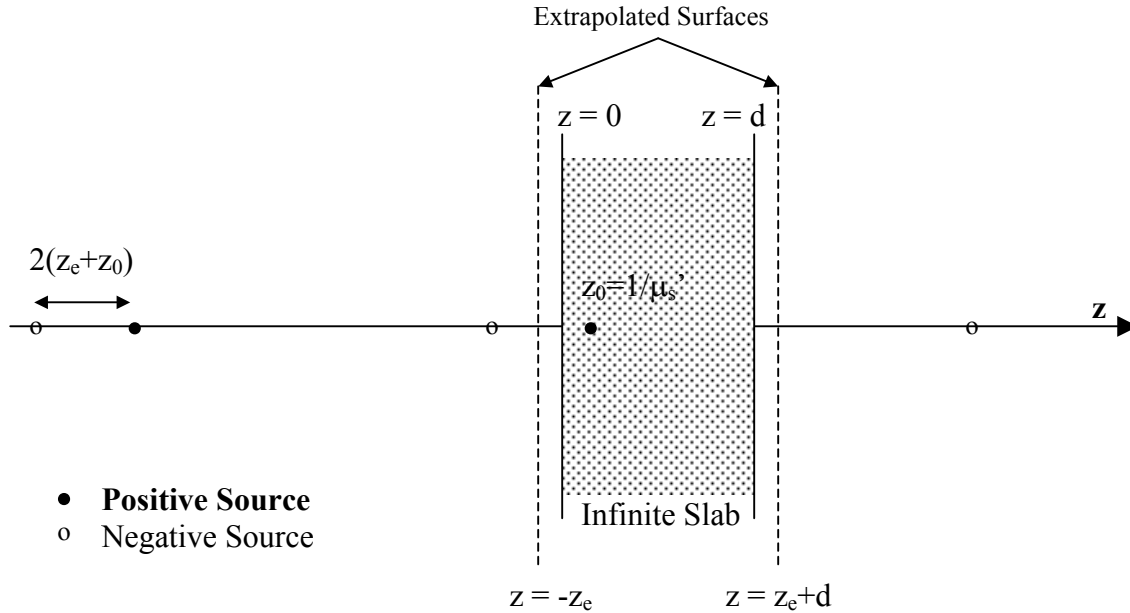


Figure 2.3 The source position is shown a distance  $z_0$  inside the tissue boundary for the extrapolated boundary condition (EBC). The average intensity is assumed to be zero at a distance  $z_e$  from the boundary. A negative image charge is shown reflected about the  $z = -z_e$  boundary. Other dipole sources are shown as part of an infinite series of dipoles.

$$T_{ZBC}(\rho, z = d, t) = (4\pi D)^{-3/2} t^{-5/2} \exp(-\mu_a \nu t) \exp\left(-\frac{\rho^2}{4Dt}\right).$$

$$\sum_{m=0}^{m=\infty} \left\{ [(2m+1)d - z_0] \exp\left(-\frac{[(2m+1)d - z_0]^2}{4Dt}\right) - [(2m+1)d + z_0] \exp\left(-\frac{[(2m+1)d + z_0]^2}{4Dt}\right) \right\} \quad (2.15)$$

The geometry for the calculation of the time resolved transmittance for a homogeneous slab for the EBC is shown in Figure 2.3. The average diffuse intensity is assumed to be zero at an extrapolated boundary located at  $z = -z_e$ . The EBC also assumes an isotropic source located a distance  $z = z_0$  inside the boundary of the homogeneous slab [2,3]. The boundary condition is met at the first surface by adding a negative source at

the position  $z = -(z_e + z_0)$ . Like for the case of the ZBC, the boundary conditions are not met with just one dipole, but with an infinite number located at

$$z_{+,m} = 2m(d + 2z_e) + z_0 \quad \text{for positive sources, and} \quad (2.16)$$

$$z_{-,m} = 2m(d + 2z_e) - 2z_e - z_0 \quad \text{for negative sources}$$

$$\text{where } m = (0, \pm 1, \pm 2, \dots).$$

The transmittance of an infinite slab with the EBC is given by Contini *et al.* [3] as

$$T_{EBC}(\rho, z = d, t) = (4\pi D)^{-3/2} t^{-5/2} \exp(-\mu_a \nu t) \exp\left(-\frac{\rho^2}{4Dt}\right) \cdot \sum_{m=-\infty}^{m=\infty} \left\{ z_{1,m} \exp\left(-\frac{z_{1,m}^2}{4Dt}\right) - z_{2,m} \exp\left(-\frac{z_{2,m}^2}{4Dt}\right) \right\} \quad (2.17)$$

where

$$z_{1,m} = d(1 - 2m) - 4mz_e - z_0$$

$$z_{2,m} = d(1 - 2m) - (4m - 2)z_e + z_0$$

$$\text{where } m = (0, \pm 1, \pm 2, \dots).$$

Contini *et al.* [3] showed that there are significant differences between the results of the ZBC and the EBC in the case of transmittance through an infinite slab. The TPSF for the ZBC (independent of  $n$ ) showed an intensity significantly lower, the maximum occurs at shorter times, and the slope at longer times is larger with respect to the EBC. It has been shown for the EBC that  $\mu_s'$  may be overestimated by 10-20% and values of  $\mu_a$  underestimated by the order of 10% for conditions typical for a compressed breast. It is clear that a reliable model for inversion procedures should account for the effect of reflections at the boundary for the case of transmission measurements on a diffusing slab.

The differences between the results of the boundary conditions can be explained by the redistribution of photons inside the slab due to reflections at the boundaries. For the case of  $n = 1.4$ , more than 50% of the photons are reflected if an isotropic distribution for the radiance is assumed. These photons continue to migrate through the slab. Thus, the probability of photons exiting at longer distances and longer times is increased over the ZBC.

For the case of reflection, there are significant differences in the intensity between the ZBC and the EBC. The shapes, however, are substantially similar [3]. In practice, it is difficult to measure absolute intensity, so in addition to fitting for the optical properties, one would fit for the zero time and amplitude of the TPSF, i.e., source-detector weight fitting. This implies that it is the shape and not the magnitude of the TPSF that is important in the determination of the optical properties. Thus, for the case of reflection, the ZBC results will be nearly indistinguishable from those of the EBC case for large source-detector separations. The ZBC will deviate sooner, however, than the EBC from the actual value as the source-detector separation becomes small.

#### **2.1.4 The Heterogeneous Solution of the Diffusion Equation by the Perturbation Approach.**

The analysis of the above sections assumed a homogeneous scattering and absorbing medium. Perturbation analysis represents a widely used method for evaluating small heterogeneities buried within an otherwise homogeneous medium [4,5,11-13]. A first order perturbation treatment of the diffusion equation indicates that a localized change in absorption or scattering behaves like a new source term for which the effect can be

determined by a Green's function approach. The perturbation to the photon distribution is expressed as an integration over the areas where the changes in absorption or scattering have occurred. The general condition of validity for this approximation is that the perturbation should not vary significantly from the background optical properties.

The homogeneous diffusion approximation given in Equation (2.6)

$$\left(-D_0\nabla^2 + \nu\mu_{a_0} + \frac{\partial}{\partial t}\right)\phi(\mathbf{r}, t) = \nu S(\mathbf{r}, t) \quad (2.18)$$

where the zero subscripts denote the homogeneous diffusion and absorption coefficients, can be written to take account of the dependency of the diffusion coefficient and absorption coefficient on position by considering that small perturbations  $\delta\mu_a(\mathbf{r})$  and  $\delta D(\mathbf{r})$  in the absorption coefficient and the diffusion coefficient, respectively, result in a change  $\delta\phi(\mathbf{r}, t)$  in the photon fluence such that

$$\left(-[D_0 + \delta D(\mathbf{r})]\nabla^2 + \nu[\mu_{a_0} + \delta\mu_a(\mathbf{r})] + \frac{\partial}{\partial t}\right)[\phi(\mathbf{r}, t) + \delta\phi(\mathbf{r}, t)] = \nu S(\mathbf{r}, t). \quad (2.19)$$

Subtraction of Equation (2.18) from Equation (2.19) gives

$$\left[-D_0\nabla^2 + \nu\mu_{a_0} + \frac{\partial}{\partial t}\right]\delta\phi(\mathbf{r}, t) = [\nabla \cdot \delta D(\mathbf{r})\nabla - \nu\delta\mu_a(\mathbf{r})] \cdot [\phi(\mathbf{r}, t) + \delta\phi(\mathbf{r}, t)]. \quad (2.20)$$

This perturbation equation is analogous to the diffusion Equation (2.18). The source term now depends on the strength and distribution of the perturbation. The first Born approximation consists of dropping the  $\delta\phi(\mathbf{r}, t)$  from the source term under the condition that  $\delta\phi(\mathbf{r}, t) \ll \phi(\mathbf{r}, t)$ . The perturbation can be shown to have the form [11]

$$\delta\phi(\mathbf{r}, t) = \delta\phi_a(\mathbf{r}, t) + \delta\phi_D(\mathbf{r}, t) \quad (2.21)$$

where

$$\delta\phi_a(\mathbf{r}, t) = \int \frac{\nu\delta\mu_a(\mathbf{r}')}{D} d\mathbf{r}' \left[ \int_0^t G_0(\mathbf{r}_d - \mathbf{r}', t - t') G_0(\mathbf{r}' - \mathbf{r}_s, t') dt' \right] \quad (2.22)$$

and

$$\delta\phi_D(\mathbf{r}, t) = \int \frac{\nu\delta D(\mathbf{r}')}{D} d\mathbf{r}' \left[ \int_0^t \nabla G_0(\mathbf{r}_d - \mathbf{r}', t - t') \cdot \nabla G_0(\mathbf{r}' - \mathbf{r}_s, t') dt' \right] \quad (2.23)$$

where  $G_0$  represents the Green's function for a homogeneous slab given by [3]

$$G_0(\mathbf{r}, t) = \nu(4\pi Dt)^{-3/2} \exp(-\mu_a \nu t) \exp\left(-\frac{|\mathbf{r}_d|^2}{4Dt}\right) \sum_{m=-\infty}^{m=+\infty} \left\{ \exp\left[-\frac{(z - z_{+,m})^2}{4Dt}\right] - \exp\left[-\frac{(z - z_{-,m})^2}{4Dt}\right] \right\} \quad (2.24)$$

where the summation over positive and negative dipole image sources is given by

$$\begin{aligned} z_{+,m} &= 2m(d + 2z_e) + z_0 && \text{for positive sources,} \\ z_{-,m} &= 2m(d + 2z_e) - 2z_e - z_0 && \text{for negative sources,} \\ m &= (0, \pm 1, \pm 2, \dots). \end{aligned} \quad (2.25)$$

The source pulse of light is assumed to be at time  $t = 0$ . The detector, source and voxel position vectors are given by  $\mathbf{r}_d$ ,  $\mathbf{r}_s$  and  $\mathbf{r}'$ , respectively.

Within the Born approximation, changes in absorption and scattering effect the distribution of light both linearly and independently [11]. A heterogeneity of finite volume is expected to saturate at a finite level as it differs more and more from the background optical properties. This behavior is inconsistent with the linear dependency predicted by Equation (2.21). The Born approximation thus overestimates the change

$\delta\phi(\mathbf{r}, t)$  resulting from large perturbations from the background properties. This accuracy can be improved through iterative approaches [5].

The forward problem can be simplified by pre-calculating the ‘‘Forward Matrices’’  $A_a$  for absorption and  $A_D$  for scattering as

$$A_a(\mathbf{r}_d, \mathbf{r}_s, \mathbf{r}', t) = \int_0^t G_0(\mathbf{r}_d - \mathbf{r}', t - t') G_0(\mathbf{r}' - \mathbf{r}_s, t') dt' \quad (2.26)$$

$$A_D(\mathbf{r}_d, \mathbf{r}_s, \mathbf{r}', t) = \int_0^t \nabla G_0(\mathbf{r}_d - \mathbf{r}', t - t') \cdot \nabla G_0(\mathbf{r}' - \mathbf{r}_s, t') dt' \quad (2.27)$$

for all values of  $\mathbf{r}_d$ ,  $\mathbf{r}_s$ ,  $\mathbf{r}'$ , and  $t$ . The calculation assumes *a priori* knowledge of the background optical properties. The forward matrix must take into account the impulse response of the measurement system and can do so by convolution. The fluence attributable to the heterogeneity will now be given by

$$\delta\phi_a(\mathbf{r}, t) = -\int r' \delta\mu_a(\mathbf{r}') dr' A_a(\mathbf{r}_d, \mathbf{r}_s, \mathbf{r}', t) \quad (2.28)$$

$$\delta\phi_D(\mathbf{r}, t) = -\int r' \delta D(\mathbf{r}') dr' A_D(\mathbf{r}_d, \mathbf{r}_s, \mathbf{r}', t) \quad (2.29)$$

The magnitude of the scattered field for both absorption and scattering depend on the product of the heterogeneity volume and  $\delta\mu_a$  or  $\delta D$ , respectively [4]. Thus, it is not possible to determine both the size and magnitude of the heterogeneity simultaneously in the linear approximation. Boas points out that in general, at least three moments need to be detectable to permit full characterization of the heterogeneity [14].



### 2.1.5 The Inverse Problem and Image Reconstruction

The Equations (2.28) and (2.29) for the fluence resulting from an absorption or scattering heterogeneity can be discretized to yield the following system of linear equations

$$\begin{bmatrix} \delta\phi_a(\mathbf{r}, t) \\ \delta\phi_D(\mathbf{r}, t) \end{bmatrix} = \begin{bmatrix} A_a(\mathbf{r}_d, \mathbf{r}_s, \mathbf{r}', t) \\ A_D(\mathbf{r}_d, \mathbf{r}_s, \mathbf{r}', t) \end{bmatrix} \begin{bmatrix} \delta\mu_a(\mathbf{r}, t) \\ \delta D(\mathbf{r}, t) \end{bmatrix} \quad (2.30)$$

This linear system is ill-posed and underdetermined. Therefore, some type of regularization or stabilization technique is required. Several techniques have been implemented including algebraic approaches consisting of the Algebraic Reconstruction Technique (ART) and a modification of ART referred to as the Simultaneous Iterative Reconstruction Technique (SIRT), subspace approaches including Truncated Singular Value Decomposition (TSVD) and Truncated Conjugate Gradient (TCG), and regularization approaches such as the classic Tikhonov regularization [4].

The Time-Domain Breast Imaging System makes use of the SIRT algebraic method. The large number of measurements resulting from the multiple time gates makes matrix inversion techniques impractical due to computer memory limitations. SIRT is a variation of ART that sequentially projects estimates onto a hyperplane defined by a particular row of the linear system [5,15]. In general, SIRT generates smoother reconstruction of the object function relative to ART, as it averages over a number of projections. This comes, however, at the expense of slower convergence. The SIRT algorithm can be expressed as

$$\mathbf{x}_i = \mathbf{x}_{i-1} - \left[ \frac{\mathbf{x}_{i-1}^T \mathbf{a}_j - b_j}{\mathbf{a}_j^T \mathbf{a}_j} \right] \mathbf{a}_j \quad (2.31)$$

for the linear system  $\mathbf{a} \cdot \hat{\mathbf{x}} = \mathbf{b}$ , where  $b_j$  represents the set of measurements,  $\mathbf{a}_j$  represent the A weights of the forward matrix, and  $\mathbf{x}_i$  represent the set of unknown object functions. One of the primary advantages of using algebraic techniques instead of matrix inversion is that hard constraints can be used, given some *a priori* knowledge, such as the reconstructed absorption should always be positive. For instance, at the end of each SIRT iteration, any voxel with negative absorption could be assigned a zero magnitude. As mentioned, above, the  $\delta\mu_a$  and  $\delta D$  – volume products are conserved within the first Born approximation. The SIRT algorithm moves through a family of solutions with increasing absorption or scattering with decreasing volume as the number of iterations increases [5]. Thus, one must make some reasonable guess as to when the number of iterations both maximizes the contrast-to-noise ratio and is representative of expected size and optical properties. One tool that has been shown to help is the L-Curve analysis, which plots the residual between the measured and theoretical optical properties and the image norm.

## 2.2 Breast Tissue Anatomy and Optical Properties

The anatomy of the female breast is described to derive insight into tissue structures and characteristics that may provide optical contrast. Both benign and cancerous lesions of the breast are described along with the four primary chromophores relevant to optical imaging. The breast tissue is shown to have low concentrations of hemoglobin relative to other tissue types. The concentrations of lipids and water are shown to be in relative abundance in the breast. Thus, errors would arise in the determination of blood volume

and oxygen saturation if lipids and water were to be ignored as they often can be in other tissue types.

### 2.2.1 Breast Tissue Anatomy

The human female breast has a very complex anatomy and physiology that can be quite variable depending on age, hormonal status, lifestyle and genetic background [21-24]. Thus, it is difficult to define “normal” breast tissue, as the organ is constantly changing. Some generalizations can be made, such as changes that occur with age. This discussion begins with the anatomy of the “normal” pre-menopausal female breast, followed by a discussion of changes that occur due to menopause. The sources of optical contrast for both absorption and scattering are described. This section concludes with a discussion of both the benign and cancerous lesions that can occur along with their associated optical contrast.

The primary anatomical structures of the female breast are indicated in cross sectional and perspective views in Figure 2.4. The breast is a bilateral organ found in the

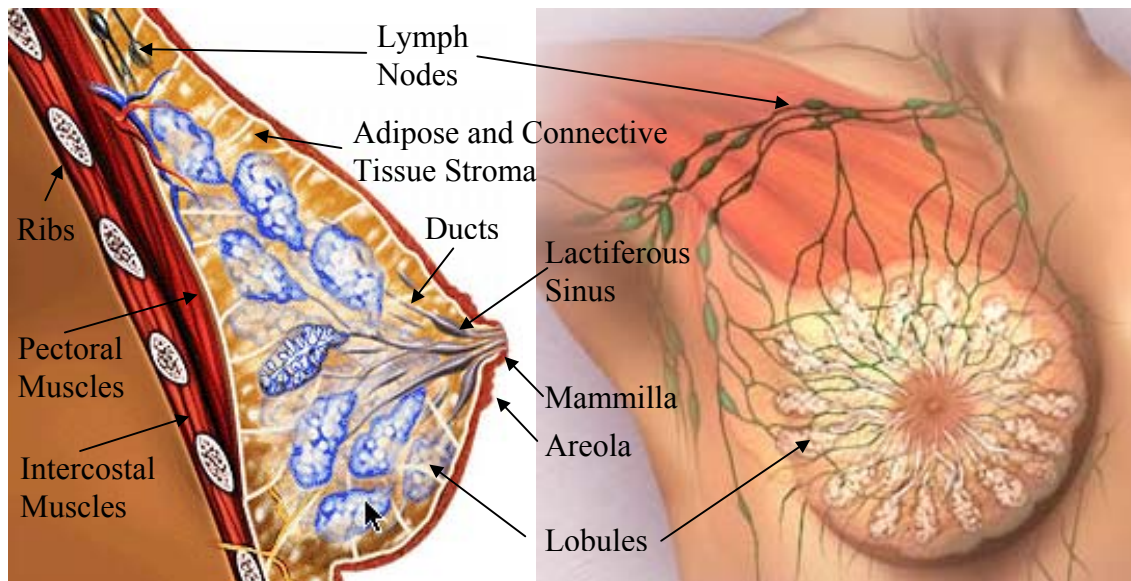


Figure 2.4 The anatomy of the female breast is shown in cross section on the left and in perspective view on the right.

skin and subcutaneous tissues of the anterior chest [21,22]. The skin consists of two primary layers. The superficial epidermis contains keratins and melanin. The underlying dense collagenous dermis contains a rich plexus of dermal blood and lymphatic vessels that lie close to the skin surface. Adipose tissue (fat) lies beneath the skin, which covers, surrounds, and intermixes with the light pinkish-tan breast glandular tissue and its white fibrous tissue stroma (Cooper's ligaments). Adipose tissue is bright yellow in adult humans due to the accumulation of carotene in the lipids and fat cells. The breast is generally well supplied with blood, but more vessels are found in the glandular than in the fibrous or adipose stroma. Lymphatic vascular channels course through the skin and breast tissues draining interstitial (edema) fluids in both the normal and diseased breast. Additionally, the breast tissue and skin are supplied with numerous small nerves.

The lobule is the basic functional unit of the glandular breast and is formed of convoluted tubular ducts surrounded by an ellipsoidal volume of loose fibrous connective tissue [21,22]. Lobules vary in size from about 0.05 to 0.3 -0.5 cm in the greatest dimension depending on hormonal status. Clusters of lobules empty into interlobular ducts and then into larger extralobular ducts. The lobular clusters and their associated duct systems form into 15 – 20 lobes. Each of the lobes is drained by one large lactiferous duct that travels to the mammilla (nipple) for the discharge of milk in the lactating breast. The Cooper's ligaments consist of bands of dense fibrous collagenous tissue that form a 3-dimensional scaffolding extending from the dermis to the subcutaneous fascia, a thin fibrous sheet separating the breast tissue from the underlying muscles of the chest. Adipose tissues are intermixed in varying amounts within the glandular breast stroma, depending on a patient's body mass index (BMI), age, genetics

and lifestyle. The BMI scale is determined by dividing the body mass (Kg) by height squared (m). Numbers between 20 and 25 are considered normal [23]. There is a general increasing trend in breast lipid mass density with increasing BMI.

The lobular ducts are lined with a two-cell layer of glandular epithelium, which along with the surrounding loose fibrous stroma, undergoes considerable changes in response to hormones produced during the 28-day menstrual cycle or in pregnancy and lactation. Blood flow can increase by 50% at the time of ovulation (midcycle) and remains high until menstruation. Some women experience as much as a 20% enlargement of their breasts by the end of their monthly cycle. This enlargement resolves during the period of menstrual bleeding when ovarian hormones are at their lowest levels.

The lobules become enlarged during pregnancy by ductal proliferation and differentiation into secretory units in response to continued high levels of hormones produced by the ovary, pituitary and placenta [21]. The glandular breast volume is more dominant than that of the compressed fibrous and fat stroma by the time the baby is born. The large lobular clusters become engorged with milk during lactation. The glandular breast volume continues to dominate as long as lactation continues.

The breast lobules atrophy over a long period due to the cessation of ovarian hormonal function associated with menopause (45-55 years of age), unless the woman takes exogenous hormones (estrogen and progesterone) [21]. The average total volume of the lobular component shrinks from a peak of 25 – 35% at 35 years of age to less than 5% after 60 years of age. The relative fat and fibrous stroma volumes remain variable after menopause, but there is a general increase in both components with a predominance of adipose tissue after 60 years of age.

### 2.2.2 The Nature of Scattering in Breast Tissue

The scattering of visible and near-infrared photons in breast tissue is a consequence of localized differences in the index of refraction of cellular and extracellular components [21,25]. Cellular components include membrane-bound subcellular organelles such as the nuclei (6 – 8  $\mu\text{m}$  in noncancerous breast epithelial cells), mitochondria (< 1  $\mu\text{m}$ ), secretory vacuoles (1 – 10  $\mu\text{m}$ ), and other similarly sized intracytoplasmic granules. These components influence scattering due to differences in refractive index at membrane interfaces. The macroscopic average refractive index of most tissues lies between 1.38 and 1.41 in the near infrared [25]. Adipose tissue, however, has a refractive index of approximately 1.46. Microscopically, the refractive index of tissue varies spatially, with a lower refractive index in the cytosol, which is primarily an aqueous solution of salts and proteins with  $n = 1.38$ , and higher in the membrane structures with  $n = 1.48$ , consisting of phospholipid bilayers. The majority of scattering has been shown by Mie theory to be due to structures within the cell as opposed to the cell membrane [25]. The cell membrane has been shown to be responsible for the scattering at small angles, the nucleus for slightly larger angles, while the more isotropic scattering is due to small organelles within the cell, such as mitochondria. Scattering decreases with increasing wavelength to varying degrees depending on the size of the scattering centers. The scattering power (exponent dependence on the wavelength) is bounded between about slightly over 1 for Mie theory (scattering center size on order of wavelength) and 4 for Rayleigh scattering (scattering center size much less than the wavelength), although on average the exponent is closer to 1. Scattering by tissue is generally quite anisotropic (forward scattering) due to the size and elongated shape of the scattering centers.

### 2.2.3 Absorption in Breast Tissues

The most important absorbers (chromophores) in the human breast are hemoglobin, melanin, water, lipids, carotene, proteins and DNA [21,23,25]. In the near infrared part of the spectrum, carotene, proteins and DNA have negligible absorption. The epidermal cells, located at the junction of the epidermis and dermis, contain melanin densely packed into organelles called melanosomes. Melanin is a highly absorptive pigment that is particularly prominent in patients with dark skin. It is difficult to measure absolute intensity for any given source and detector pair in optical tomography, so source and detector weights are generally fitted for in the reconstruction algorithms. The extinction coefficient of melanin is relatively flat in the near infrared with no observed peaks and decreases somewhat with increasing wavelength [25]. Since melanin is substantially localized in the outer dermal layers of the breast, its attenuating effect could be fit for in much the same way that attenuation due to differences in optical fiber transmission or detector-to-detector sensitivity are fit for. This leaves hemoglobin, lipids, and water as the primary chromophores in the physiological window between about 650 and 1000 nm.

Lying just beneath the epidermis is a vascular, blood-rich dermis in which small arteries, veins, and capillaries form dense networks close to the epidermis. Thus, both melanin and hemoglobin are concentrated in well-defined layers within the first 1 to 2 mm of the skin surface. Thus, the effects of the hemoglobin in this superficial layer can be corrected for, as was melanin, because the fitting parameters are wavelength dependent.

The upper layer of adipose tissue lies just below the dermis. The blood supply and flow is greater in the deeper lying glandular areas in comparison to the adipose tissue.

Blood flow in the glandular breast varies during the menstrual cycle, pregnancy, and lactation [21]. The density of blood vessels decreases in the breast as a woman ages and post-menopausal atrophy sets in.

#### **2.2.4 Benign Breast Lesions**

Fibroadenomas are the most frequent of benign breast tumors occurring in about 10% of adult women [21]. Fibroadenomas are firm, circumscribed, light tan nodules formed as a result of proliferation of fibroblasts, fibrous breast lobular stroma, and to a lesser extent, breast ducts [21,22]. They tend to appear first in young women, persisting as the woman ages, sometimes fluctuating in size relative to age. Frequently, fibroadenomas are surrounded by lesions of fibrocystic disease of the breast. Very infrequently, fibroadenomas can harbor noninvasive or invasive carcinomas, cancers that arise from the breast ductal epithelium. The most prominent fibroadenoma chromophores would be water and hemoglobin. Essentially no adipose tissue is found in fibroadenomas. Thus, relative to background optical properties, fibroadenomas would be expected to have higher absorption and higher scattering.

Fibrocystic disease or fibrocystic change of the breast covers a broad spectrum of benign localized or diffuse stromal and glandular alterations that can produce diffuse masses, distinct tumors, and/or nonpalpable lesions. The greatest problem that fibrocystic change presents to diagnostic imaging is that many of the ductal proliferative lesions mimic the anatomic structure of cancers [21]. In fact, many cancers can be obscured by the fibrocystic disease. The 'dense breast' that causes difficulty in X-ray mammography is usually due to the dense fibrosis of fibrocystic change. Microscopic



calcifications can be present in fibrocystic disease although, most of the time, the distribution and size of the calcifications are different from those of cancer calcifications. In general, the most likely optical contrast due to fibrocystic disease would manifest as increased scattering.

Benign fluid filled cysts that may be due to apocrine metaplasia of the lobular acinar epithelium can range in size from microscopic to many cubic centimeters in volume [22]. The increased secretion of the cells is not balanced by increased resorption, resulting in dilation of the lobule. The generally dark brown fluid found in the cysts contains degenerated cells, secretions and blood that may or may not have distinctive absorption properties. Cysts are likely to be characterized by significantly lower scatter, however, relative to the background.

Lipomas are benign fat tumors comprised of mature adipose cells. These yellow lesions generally have similar scattering characteristics as the surrounding fat, but may have more blood vessels, which could provide optical contrast relative to surrounding fat [21].

### **2.2.5 Cancers of the Breast**

Cancer is the culmination of a series of genetic events that lead to unchecked proliferation of cells in a primary site followed by further genetic mutations that allow these cells to invade into surrounding tissues, breach the walls of blood vessels and lymphatics to travel to distant tissues and establish new growth (metastases) in these distant tissues [22]. Cancer cells are not recognized as belonging to the host and will thereby elicit immune responses. They can secrete various growth factors and cytokines

that stimulate host responses of inflammation, blood vessel proliferation (cancer related angiogenesis) and fibrosis (desmoplasia). Some cancers, including breast carcinomas, elicit substantial host responses. Tumors formed by these cancers can be as much as 90% non-cancerous host cells and tissues with dense fibrous connective tissue predominating. Thus, the diagnostically important chromophores of cancers can be found either in the cancer cells themselves or in the tissues of the host response to the malignant growth.

Carcinoma is the most frequent cancer of the female breast and is derived from the epithelium of the breast ducts and lobules. Ductal carcinomas are thought to have their origin in the larger intra- and extra-lobular ducts, while lobular carcinomas are thought to originate in the terminal lobular glandular ducts [21,22]. Carcinomas are also classified according to their location. Carcinomas confined within the ducts and lobular glands are called ductal carcinoma *in situ* (DCIS) and lobular carcinoma *in situ*, respectively. *In situ* carcinomas have not undergone genetic changes necessary for them to invade surrounding tissue. The carcinomas are classified as infiltrating ductal carcinoma and infiltrating lobular carcinoma depending on their diagnostic histological appearances, once the cells have acquired the ability to invade. Frequently, *in situ* and invasive carcinomas are found in the same cancer mass and can be present in several sites throughout the same or opposite breast. About 85 to 90% of all infiltrating carcinomas are infiltrating ductal carcinomas, with the balance comprised of infiltrating lobular carcinomas [21].

It is likely that the success of optical diagnosis of breast carcinoma rests on the alterations produced by the tissues of the host response rather than direct detection of cancer cells [21]. The host responses include infiltrates of lymphocytes and other

inflammatory cells of immune response, desmoplasia with fibroblast proliferation and fibrosis, angiogenesis in response to fibroblastic and vascular growth factor produced by the carcinoma cells, and wound healing associated with hemorrhage. These responses can lead to scattering and absorption contrast relative to normal tissues and hold the promise of optical detection.

Angiogenesis is the formation of new blood vessels derived from surrounding existing blood vessels stimulated by various growth factors due to the genetic mutations of cancers [21]. The new vessels are generally concentrated on the periphery of the lesion forming an intertwining network resembling densely branched bushes. These new blood vessels are thin walled, dilated, lined by leaky endothelium that contains gaps exposing underlying cancer and host cells, and inclined to degenerate, leading to necrosis of the blood-deprived cancer. *In situ* and infiltrating ductal carcinomas as well as infiltrating lobular carcinomas elicit angiogenesis. A dense layer of new capillaries is stimulated to grow as a vascular cuff around the ducts containing the DCIS. In general, vascular densities are increased at the periphery and within infiltrating ductal and lobular carcinomas, but densities can show considerable variation. Thus, in general an increase in blood volume and a decrease in oxygen saturation would be expected to be associated with cancerous tumors [21,26-28].

### 2.2.6 Breast Tissue Chromophores

The wavelength dependent absorption coefficient of breast tissue is equal to the sum of the products of all significant chromophore extinction coefficients  $\varepsilon_i$  [ $\text{cm}^{-1}\text{M}^{-1}$ ] and concentrations  $C_i$  [M] as

$$\mu_a(\lambda) = \sum_1^i \varepsilon_i(\lambda) C_i \quad (2.32)$$

where a dependency on wavelength  $\lambda$  is indicated for both the absorption and extinction coefficients. The total mean transmittance  $\langle T \rangle$  experienced at a particular wavelength over a given mean path through tissue is given by the Beer-Lambert Law [29] as

$$\langle T \rangle = I / I_0 = \exp(\mu_a \langle L \rangle) \quad (2.33)$$

where  $I$  is the final intensity after passing through the tissue,  $I_0$  is the initial intensity incident on the tissue, and  $\langle L \rangle$  is the mean path through the tissue, given by  $v \langle t \rangle$  for a time-domain system where the time in brackets is the mean flight time of photons through the tissue.

The total hemoglobin concentration [THC] is given by

$$[THC] = [Hb] + [HbO] \quad (2.34)$$

where [Hb] and [HbO] are the concentration of deoxy-hemoglobin and oxy-hemoglobin, respectively [23]. Another important metabolic blood parameter is the oxygen saturation defined by [23]

$$S_t O_2 = \frac{[HbO]}{[THC]} \quad (2.35)$$

Tumors are generally associated with angiogenesis and exhibit an increase in metabolism and blood flow relative to normal tissue, especially at the tumor periphery. This would be expected to result in a decrease in oxygen saturation and an increase in total hemoglobin concentration. Thus, NIR imaging is expected to be sensitive to functional changes indicative of tumor formation.

The significant chromophores relevant to breast imaging and spectroscopy are hemoglobin, lipids, and water, as stated above in Section 2.2.3. Figure 2.5 shows the extinction coefficients for oxy- and deoxy- hemoglobin [30], lipid [25] and water [31]. The extinction coefficient of lipid was multiplied by a factor of  $5 \times 10^4$  and that of water by  $1 \times 10^6$  so that they could be displayed on the same scale.

Tissues such as adult muscle have hemoglobin concentrations on the order of 100  $\mu\text{M}$ . The concentration of hemoglobin in the breast, however, is significantly lower than in muscle, ranging from the order of 10 to 40  $\mu\text{M}$  [23,41]. Even though water has a very low extinction coefficient, it is present in the breast in molar concentrations. Lipids are also very prominent in the breast. Thus, even though both water and lipids are weak absorbers relative to hemoglobin, their high concentrations result in enough absorption to compete with hemoglobin. Failure to take proper account of water and lipids can result in an overestimation of total hemoglobin concentration on the order of 20% or more and over 5% in oxygen saturation [23]. The amount of water and lipids as well as hemoglobin concentration depends on a number of factors, such as hormonal status, age,

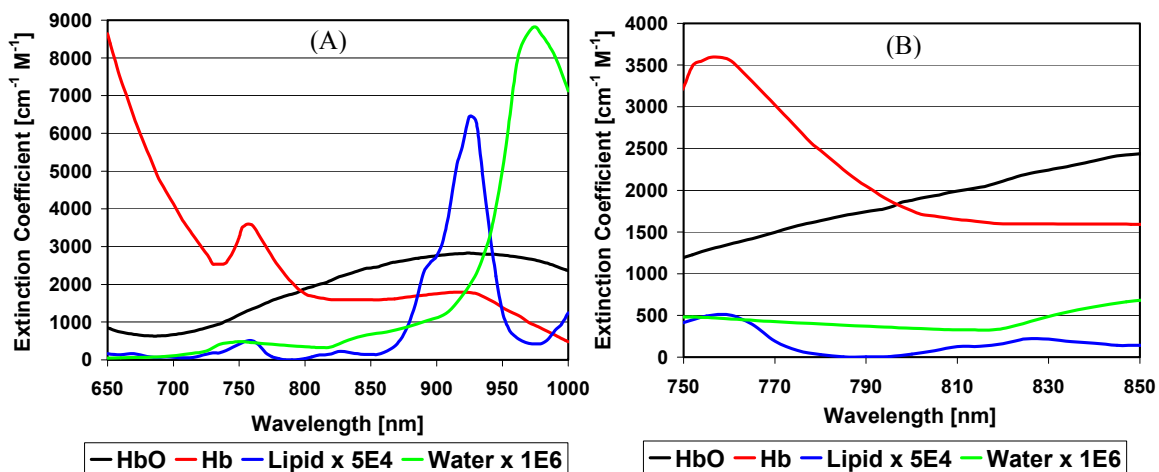


Figure 2.5 The extinction coefficients of oxy- and deoxy-hemoglobin, lipid and water are shown as the primary chromophores relevant to DOT breast imaging and spectroscopy. The lipid curve is multiplied by  $5 \times 10^4$  and the water by  $1 \times 10^6$  to register on the same scale.

and menstruation [21-23]. Following ovulation, blood flow to the breast can increase by up to 50%, the breast volume increases, and parenchymal water content changes by an average of 25% during the latter half cycle. Tissue is typically about 60% water by mass, and the mammary gland in particular may have 30-73% water by mass [23]. Lipids make up about 19% of tissue by mass, and can range from 5-56% in the mammary gland.

Figure 2.6 illustrates the substantial mean variations (sample size of 30 healthy volunteers) in breast tissue chromophores that are correlated to pre- and post-menopausal status as described by Cerussi *et al* [23]. Plots (A) and (B) of Figure 2.6 represent pre-

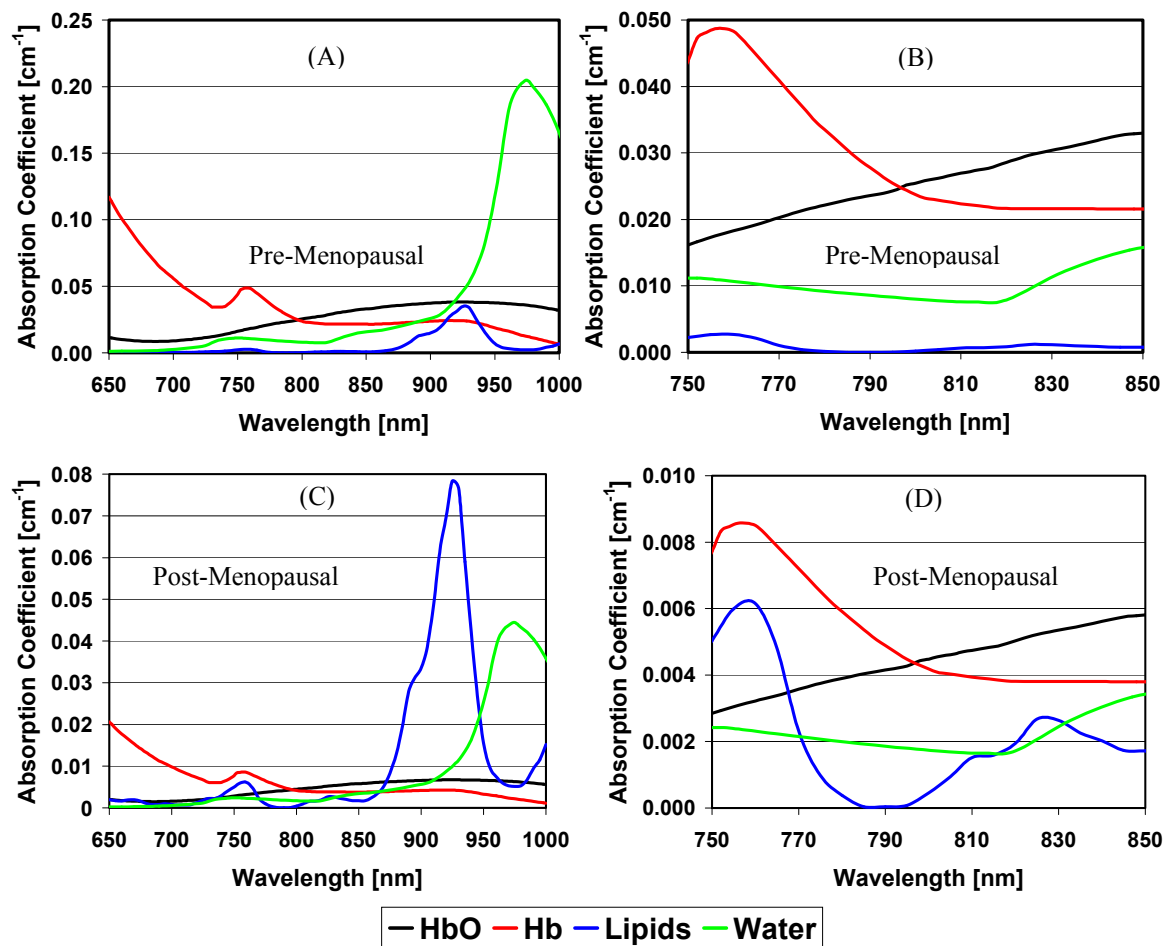


Figure 2.6 The absorption coefficient for average values for the cases of Pre- and Post-Menopausal breast tissue is shown for oxy- and deoxy-hemoglobin, lipids, and water chromophores. Substantial average differences are observed between the two cases. This data shows that, in the case of imaging or spectroscopy on breast tissue, it is important to consider the affects of lipid and water.

menopausal status, representative of women typically under 50 years of age. Plots (C) and (D) of Figure 2.6 represent post-menopausal status, typical of women over the age of 50. Pre-menopausal spectra show significantly higher concentrations of hemoglobin and more water relative to lipids in comparison with post-menopausal spectra. The pre-menopausal breast has a greater density of vascular glandular tissue in comparison to the post-menopausal breast for which the glandular tissue begins to atrophy into fatty tissue because of the cessation of ovarian estrogen production [21,23]. The data also indicates an increase in oxygen saturation for post-menopausal breast tissue, which may be indicative of reduced metabolic requirements. Cerussi *et al.* also point out that there is a decrease in the mean scattering coefficient on the order of 30% for post-menopausal relative to pre-menopausal tissue. This change in scattering would be consistent with a change in breast structure associated with menopause. Cerussi *et al.* point out that the wide variations in the data due to menstrual cycle differences and gynecological age, decrease substantially around the age of 50 to 55. The study suggests that neglecting the effect of water and lipids has the effect of making it appear that there is more oxygenated blood in the breast tissue. The problem may be particularly acute for the case of the post-menopausal breast as indicated by plot (D) of Figure 2.6.

The practical limitations of the instrumentation used to assess the optical properties of breast tissue must be considered. In particular, the Time-Domain Breast Imaging System of this dissertation is limited to wavelengths between 750 and 850 nm by the range of the Spectra-Physics Ti:Sapphire laser. Additionally, many of the detector systems used in DOT that employ photomultiplier technology fall off precipitously in response beyond about 850 nm. With reference to plots (B) and (D) of Figure 2.6, the

lipid spectrum is shown to have an absorption peak very close to that of deoxy-hemoglobin near 760 nm. Lipid also shows a minimum near 790 nm and another peak near 825 nm. Water, on the other hand, has very little structure and is relatively flat in its absorption spectrum over the 750 to 850 nm spectrum. Also, note that the relative proportion of water in comparison with hemoglobin is similar for both the pre- and post-menopausal breast. Franceschini *et al.* [32] have suggested a correction factor to the total absorption coefficient in the breast, assuming a water concentration of 70%. While this general approach seems reasonable for the case of the pre-menopausal breast, it may be expected to lead to quantitative errors in the case of post-menopausal breast as indicated in plot (D) of Figure 2.6. The practical limitations imposed by patient tolerance on clinical measurement time, however, may restrict measurements to just two to three wavelengths. Thus, it may not be feasible to derive concentrations of oxy- and deoxy-hemoglobin, lipids, and water from measured data. In that case, the approach suggested by Franceschini *et al.* may be the best general approach. The *a priori* knowledge of a patient's gynecological age could be used to apply some typical correction factor for both lipids and water. This approach would not account for the significant variations observed for pre-menopausal breasts, but it would likely offer improved quantitative accuracy over the approach of totally neglecting the effects due to lipids and water in the breast.

One source of quantitative error in the calculated oxygen saturation values generally overlooked in the literature is due to the presence of carboxyhemoglobin (HbCO). Carbon monoxide has a significantly higher affinity for hemoglobin in comparison with oxygen. It binds with hemoglobin and prevents association with oxygen, thereby depressing the oxygen saturation. The extinction of HbCO is significantly reduced and



distinct from that of HbO in the near infrared. The fraction of hemoglobin in the form of HbCO is generally sufficiently low, on the order of 1.5%, as to be negligible. For heavy smokers, however, the fraction can be as high as 15% and can significantly affect the determination of blood volume and saturation [33-35]. It can lead to an overestimation of oxygen saturation in the case of a heavy smoker on the order of several percent. Unfortunately, accurate quantification of HbCO would require a multi-wavelength, multi-component analysis, which as mentioned above, is not always clinically feasible, given limitations of maximum acquisition time and limitations of the instrumentation.

If the only two chromophores considered are oxy- and deoxy-hemoglobin [32,36-38], then a minimum of two wavelengths are required for the determination of [Hb] and [HbO]. From Equation (2.32)

$$\mu_a^{\lambda_1} = [Hb]\varepsilon_{Hb}^{\lambda_1} + [HbO]\varepsilon_{HbO}^{\lambda_1} \quad (2.36)$$

$$\mu_a^{\lambda_2} = [Hb]\varepsilon_{Hb}^{\lambda_2} + [HbO]\varepsilon_{HbO}^{\lambda_2} \quad (2.37)$$

where  $\mu_a^{\lambda_1}$  and  $\mu_a^{\lambda_2}$  are the absorption coefficients at wavelengths  $\lambda_1$  and  $\lambda_2$ , respectively,  $\varepsilon_{Hb}^{\lambda_1}$  and  $\varepsilon_{Hb}^{\lambda_2}$  are the extinction coefficients for deoxy-hemoglobin at wavelengths  $\lambda_1$  and  $\lambda_2$ , respectively, and  $\varepsilon_{HbO}^{\lambda_1}$  and  $\varepsilon_{HbO}^{\lambda_2}$  are the extinction coefficients of oxy-hemoglobin at wavelengths  $\lambda_1$  and  $\lambda_2$ , respectively. This set of two equations and two unknowns is easily solved for the concentrations of oxy- and deoxy-hemoglobin as

$$[Hb] = \frac{\mu_a^{\lambda_1}\varepsilon_{HbO}^{\lambda_2} - \mu_a^{\lambda_2}\varepsilon_{HbO}^{\lambda_1}}{\varepsilon_{Hb}^{\lambda_1}\varepsilon_{HbO}^{\lambda_2} - \varepsilon_{Hb}^{\lambda_2}\varepsilon_{HbO}^{\lambda_1}} \quad (2.38)$$

$$[HbO] = \frac{\mu_a^{\lambda_2}\varepsilon_{Hb}^{\lambda_1} - \mu_a^{\lambda_1}\varepsilon_{Hb}^{\lambda_2}}{\varepsilon_{Hb}^{\lambda_1}\varepsilon_{HbO}^{\lambda_2} - \varepsilon_{Hb}^{\lambda_2}\varepsilon_{HbO}^{\lambda_1}} \quad (2.39)$$

The total hemoglobin concentration [THC], i.e. blood volume, is readily determined from Equation (2.34) and the oxygen saturation  $S_tO_2$ , from Equation (2.35). Equation (2.32) could readily be extended to include multiple wavelengths and multiple chromophores. Multivariate linear regression and principal components analysis techniques can be used to solve the system of linear equations, particularly when one analyte has an effect on another, such as would be the case for the several forms of hemoglobin [33,34,39,40].

Optical tomography often does not determine the absolute concentrations of hemoglobin or the absolute absorption coefficients, rather the change  $\Delta[Hb]$ ,  $\Delta[HbO]$ , and  $\delta\mu_a$  [36]. The forward models assume a small perturbation of  $\delta\mu_a$  on an otherwise homogeneous background. Errors in the determination of the background optical properties could lead to significant errors in the reconstructed images [37].

The simplifying assumption that breast tissue is homogeneous limits the validity of DOT. Some investigators have modeled structured layers [17,32], but even these models can't account for large asymmetric heterogeneous regions that may more accurately reflect real breast tissues. More precise imaging will likely require more sophisticated models in the future.

### 2.2.7 Optical Properties of Breast Tissue

A study of 52 healthy female breast tissues was measured *in vivo* in parallel plate transmission geometry to establish data for the range of optical properties [41]. The instrument was based on frequency-domain techniques at a modulation frequency of 140 MHz and wavelengths of 750, 786, and 830 nm. The absorption coefficients  $\mu_a$ , varied from just under  $0.02 \text{ cm}^{-1}$  to  $0.08 \text{ cm}^{-1}$ , with a mean of  $0.41 \pm 0.025 \text{ cm}^{-1}$  at 786 nm. The

reduced scattering coefficients  $\mu_s'$  varied from 4 to 14  $\text{cm}^{-1}$  at 786 nm with a mean of  $8.5 \pm 2.1 \text{ cm}^{-1}$ . Blood oxygen saturation varied from 50 to 80 % with a mean of  $68 \pm 8 \%$ , while blood volume ranged from 10 to 50  $\mu\text{M}$  with a mean of  $34 \pm 9 \mu\text{M}$ . The study did not supply information regarding the age, menstrual cycle or hormonal status of the women or the degree of compression, so it is difficult to assess how these factors may have skewed the data. Nevertheless, the data gives us an idea of the range of optical constants that may encountered in a clinical setting.

### 2.3 Summary

The widely used diffusion approximation to the radiative transport equation was discussed along with solutions specific to transmission through a slab applicable to breast imaging. The well-known Born approximation was used as a perturbative approach to derive analytical expressions for the scattered field due to small heterogeneities within a homogeneous slab. Methods for solving the inverse problem using SIRT techniques were also discussed.

The anatomy of the female breast was shown to be complex relative to the simple model assumptions. Sources of optical contrast for both the healthy and diseased breast were described. The absorption due to both water and lipids was shown to be significant in optical breast imaging, particularly for the post-menopausal breast. A simple method of determining hemoglobin saturation and volume based on as few as two wavelengths was described.

Finally, ranges for optical properties of the breast were discussed. Knowledge of these typical ranges is important to consider for the optimization of instrumentation design.

## Chapter 2 References

1. S. R. Arridge, M. Cope, and D. T. Delpy, "The theoretical basis for the determination of optical pathlengths in tissue: temporal and frequency analysis," *Phys. Med. Biol.* **37**, 1531-1560 (1992).
2. A. H. Hielscher, S. L. Jacques, L. Wang, and F. K. Tittel, "The influence of boundary conditions on the accuracy of diffusion theory in time-resolved reflectance spectroscopy of biological tissues," *Phys. Med. Biol.* **40**, 1957-1975 (1995).
3. D. Contini, F. Martlli, and G. Zaccanti, "Photon migration through a turbid slab described by a model based on diffusion approximation. I. Theory," *Appl. Opt.* **36**, 4587-4599 (1997).
4. D. A. Boas, "Diffuse photon probes of structural and dynamical properties of turbid media: Theory and biomedical applications," Ph.D. Dissertation, University of Pennsylvania. 1996.
5. M. A. O'Leary, "Imaging with diffuse photon density waves," Ph.D. Dissertation, University of Pennsylvania 1996.
6. M. S. Patterson, B. Chance, and B. C. Wilson, "Time resolved reflectance and transmittance for the non-invasive measurement of tissue optical properties," *Appl. Opt.* **28**, 2331-2336 (1989).
7. S. L. Jacques, "Time-resolved reflectance spectroscopy in turbid tissues," *IEEE Transactions on Biomedical Engineering* **36**, 1155-1161 (1989).
8. A. D. Klose and A. H. Hielscher, "Iterative reconstruction scheme for optical tomography based on the equation of radiative transfer," *Med. Phys.* **26**, 1698-1707 (1999).
9. J. Hebden and D. T. Delpy, "Enhanced time-resolved imaging with a diffusion model of photon transport," *Opt. Lett.* **19**, 311-313 (1994).
10. T. Durduran, A. G. Yodh, B. Chance, and D. A. Boas, "Does the photon-diffusion coefficient depend on absorption?," *J. Opt. Soc. Am. A* **14**, 3358-3365 (1997).
11. M. Morin, S. Chatigny, A. Mailloux, Y. Painchaud, and P. Beaudry, "Time-domain perturbation analysis of a scattering slab," *SPIE Proc.* **3597**, 67-78 (1999).
12. S. R. Arridge and J. C. Hebden, "Optical imaging in medicine: II. Modelling and reconstruction," *Phys. Med. Biol.* **42**, 841-853 (1997).
13. S.R. Arridge, "Chapter 1: Diffusion tomography in dense media," from Scattering in Microscopic Physics and Chemical Physics: Practical Aspects of Visible and Non-Visible Light Scattering
14. D. A. Boas, "A fundamental limitation of linearized algorithms for diffuse optical tomography," *Opt. Expr.* **1**, 404-413 (1997).
15. D. A. Boas, T. Gaudette, G. Strangman, X. Cheng, J. J. A. Marota, and J. B. Mandeville, "The accuracy of near infrared spectroscopy and imaging during focal changes in cerebral hemodynamics," *NeuroImage* **13**, 76-90 (2001).
16. A. Kienle and M. S. Patterson, "Improved solutions of the steady-state and the time-resolved diffusion equations for reflectance from a semi-infinite turbid medium," *J. Opt. Soc. Am. A* **14**, 246-253 (1997).

17. F. Martelli, A. Sassaroli, and Y. Yamada, "Analytical solution of the time-dependent photon diffusion equation for a layered medium," *SPIE Proc.* **3597**, 79-89 (1999).
18. M. Lepore, I. Delfino, A. Ramaglia, F. Vigilante, and P. L. Indovina, "An experimental comparison between time-resolved transmittance and reflectance techniques for optical characterization of scattering media," *SPIE Proc.* **3597**, 414-422 (1999).
19. F. Gao, H. Zhao, and Y. Yamada, "Improvement of image quality in diffuse optical tomography by use of full time-resolved data," *App. Opt.* **41**, 778-791 (2002).
20. M. Lepore, G. Urso, R. Esposito, L. Bottalico, M. Esposito, M. D. Falco, I. Delfino, and P. L. Indovina, "Development of a time-domain tomographic system for optical imaging," *SPIE Optical Tomography and Spectroscopy of Tissue IV* **4250**, 419-428 (2001).
21. S. Thomsen and D. Tatman, "Physiological and pathological factors of human breast disease that can influence optical diagnosis," Thomsen & Tatman: Human Breast Disease, *Annals of New York Academy of Sciences*, 171-193 (1997).
22. D. B. Kopans, *Breast Imaging*, Lippincott-Raven Publishers, Philadelphia, NY, 2<sup>nd</sup> Edition, 1998.
23. A. E. Cerussi, F. Bevilacqua, N. Shah, D. Jakubowski, A. J. Berger, R. Lanning, and B. J. Tromberg, "The effects of water and lipids on NIR optical breast measurements," *SPIE Optical Tomography and Spectroscopy of Tissue IV* **4250**, 419-428 (2001).
24. A. E. Cerussi, A. J. Berger, F. Bevilacqua, N. Shah, D. Jakubowski, J. Butler, R. F. Holcombe, and B. J. Tromberg, "Sources of absorption and scattering contrast for near-infrared optical mammography," *Acad. Rad.* **8**, 211-218 (2001).
25. C. Eker, "Optical characterization of tissue for medical diagnostics," Doctoral Thesis, Lund Institute of Technology, 1999.
26. C. J. Gullledge and M. W. Dewhirst, "Tumor oxygenation: a matter of supply and demand," *Anticancer Research* **16**, 741-750 (1996).
27. V. Quaresima, S. J. Matcher, and M. Ferrari, "Identification and quantification of intrinsic optical contrast for near-infrared mammography," *PhotoChem. and PhotoBio.* **67**, 4-14 (1998).
28. E. M. C. Hillman, "Experimental and theoretical investigations of near infrared tomographic imaging methods and clinical applications," Ph.D. Thesis, University College London, 2002.
29. M. Essenpreis, C. E. Elwell, M. Cope, P. van der Zee, S. R. Arridge, and D. T. Delpy, "Spectral dependence of temporal point spread functions in human tissues," *Appl. Opt.* **32**, 418-425 (1993).
30. Scott Prahl, Tabulated molar extinction coefficient for hemoglobin in water, Oregon Laser Medical Center, 1999.
31. K. F. Palmer and D. Williams, "Optical properties of water in the near infrared," *J. Opt. Soc. Am.*, **64**, 1107--1110, (1974).
32. M. A. Franceschini, E. Gratton, D. Hueber, and S. Fantini, "Near-infrared absorption and scattering spectra of tissues *in vivo*," *SPIE Optical Tomography and Spectroscopy of Tissue III* **3597**, 526-531 (1999).

33. A. Zwart, A. Buursma, E. J. van Kampen, B. Oeseburg, P. H. W. van der Ploeg, and W. G. Zijlstra, "A multi-wavelength spectrophotometric method for the simultaneous determination of five haemoglobin derivatives," *J. Clin. Chem. Biochem.* **19**, 457-463 (1981).
34. W. G. Zijlstra, A. Buursma, and W. P. Meeuwssen-van der Roest, "Absorption spectra of human fetal and adult oxyhemoglobin, de-oxyhemoglobin, carboxyhemoglobin, and methemoglobin," *Clin. Chem.* **37**, 1633-1638 (1991).
35. A. Zwart, E. J. van Kampen, and W. G. Zijlstra, "Results of routine determination of clinically significant hemoglobin derivatives by multicomponent analysis," *Clin. Chem.* **32**, 972-978 (1986).
36. D. A. Boas, M. A. Franceschini, A. K. Dunn, G. Strangman, "Noninvasive imaging of cerebral activation with diffuse optical tomography," Chapter 8, *In Vivo Optical Imaging of Brain Function*, CRC Press, 193-221 (2002).
37. X. Cheng and D. Boas, "Diffuse optical tomography errors resulting from uncertainty in the background optical properties," *SPIE Optical Tomography and Spectroscopy of Tissue III* **3597**, 213-220 (1999).
38. H. Liu, B. Chance, A. H. Hielscher, S. L. Jacques, and F. K. Tittel, "Influence of blood vessels on the measurement of hemoglobin oxygenation as determined by time-resolved reflectance spectroscopy," *Am. Assoc. Phys. Med.* **22**, 1209-1217 (1995).
39. S. Yeh and O. S. Khalil, "Multivariate method for the determination of tissue optical properties from diffuse reflectance profiles," *SPIE Optical Tomography and Spectroscopy of Tissue III* **3597**, 213-220 (1999).
40. R. A. Johnson and D. W. Wichern, *Applied Multivariate Statistical Analysis*, Prentice-Hall Inc., Englewood Cliffs, NJ (1992).
41. R. Choe, T. Durduran, J. P. Culver, L. Zubkov, J. M. Giammarco, X. Intes, B. Chance, and A. G. Yodh, "Bulk optical properties of normal breast with endogeneous and exogeneous contrast," *SPIE Optical Tomography and Spectroscopy of Tissue IV* **4250**, 462-464 (2001).